

The Ca²⁺ Channel Subunit β_2 Regulates Ca²⁺ Channel Abundance and Function in Inner Hair Cells and Is Required for Hearing

Jakob Neef,^{1,2,3} Anna Gehrt,^{1,4} Anna V. Bulankina,¹ Alexander C. Meyer,¹ Dietmar Riedel,⁵ Ronald G. Gregg,^{6,7} Nicola Strenzke,⁴ and Tobias Moser^{1,2,3}

¹InnerEarLab, Department of Otolaryngology and Center for Molecular Physiology of the Brain, ²Bernstein Center for Computational Neuroscience, ³Sensory and Motor Neuroscience Program, Göttingen Graduate School for Neurosciences and Molecular Biosciences, and ⁴Auditory Systems Physiology Group, Department of Otolaryngology, University of Göttingen, 37099 Göttingen, Germany, ⁵Laboratory of Electron Microscopy, Max Planck Institute for Biophysical Chemistry, 37077 Göttingen, Germany, and Departments of ⁶Biochemistry and Molecular Biology and ⁷Ophthalmology and Visual Sciences, University of Louisville, Louisville, Kentucky 40202

Hearing relies on Ca²⁺ influx-triggered exocytosis in cochlear inner hair cells (IHCs). Here we studied the role of the Ca²⁺ channel subunit Ca_v β_2 in hearing. Of the Ca_v β_{1-4} mRNAs, IHCs predominantly contained Ca_v β_2 . Hearing was severely impaired in mice lacking Ca_v β_2 in extracardiac tissues (Ca_v $\beta_2^{-/-}$). This involved deficits in cochlear amplification and sound encoding. Otoacoustic emissions were reduced or absent in Ca_v $\beta_2^{-/-}$ mice, which showed strongly elevated auditory thresholds in single neuron recordings and auditory brainstem response measurements. Ca_v $\beta_2^{-/-}$ IHCs showed greatly reduced exocytosis (by 68%). This was mostly attributable to a decreased number of membrane-standing Ca_v1.3 channels. Confocal Ca²⁺ imaging revealed presynaptic Ca²⁺ microdomains albeit with much lower amplitudes, indicating synaptic clustering of fewer Ca_v1.3 channels. The coupling of the remaining Ca²⁺ influx to IHC exocytosis appeared unaffected. Extracellular recordings of sound-evoked spiking in the cochlear nucleus and auditory nerve revealed reduced spike rates in the Ca_v $\beta_2^{-/-}$ mice. Still, sizable onset and adapted spike rates were found during suprathreshold stimulation in Ca_v $\beta_2^{-/-}$ mice. This indicated that residual synaptic sound encoding occurred, although the number of presynaptic Ca_v1.3 channels and exocytosis were reduced to one-third. The normal developmental upregulation, clustering, and gating of large-conductance Ca²⁺ activated potassium channels in IHCs were impaired in the absence of Ca_v β_2 . Moreover, we found the developmental efferent innervation to persist in Ca_v β_2 -deficient IHCs. In summary, Ca_v β_2 has an essential role in regulating the abundance and properties of Ca_v1.3 channels in IHCs and, thereby, is critical for IHC development and synaptic encoding of sound.

Introduction

The ribbon synapses of cochlear inner hair cells (IHCs) are specialized for high temporal precision and reliability of transmitter

release (Fuchs, 2005; Moser et al., 2006). Stimulus–secretion coupling builds on Ca_v1.3 L-type Ca²⁺ channels (Platzer et al., 2000; Brandt et al., 2003) that cluster at presynaptic active zones (Brandt et al., 2005) and regulate exocytosis of closely colocalized readily releasable vesicles (Brandt et al., 2005; Goutman and Glowatzki, 2007). Genetic ablation of the pore-forming (α_1D) subunit of the Ca_v1.3 channel reduces the hair cell Ca²⁺ current by >90% and results in complete deafness attributable to synaptic failure (Platzer et al., 2000; Brandt et al., 2003; Michna et al., 2003; Dou et al., 2004). Ca_v1.3 channels in IHCs are partially active at the resting potential, and the resulting tonic transmitter release drives spiking of spiral ganglion neurons in the absence of sound (Robertson and Paki, 2002). Ca²⁺–calmodulin-mediated channel inactivation is antagonized by the binding of other regulatory Ca²⁺ binding proteins (Yang et al., 2006; Cui et al., 2007).

Ca²⁺ channels are multiprotein complexes containing the transmembrane, pore-forming Ca_v α_1 subunit, a cytoplasmic Ca_v β subunit, a single-pass transmembrane subunit Ca_v $\alpha_2\delta$, and calmodulin or the Ca²⁺ binding proteins (for review, see Catterall et al., 2005). Ca_v β subunits comprise a number of protein interaction motifs and share structural properties with the membrane-

Received April 2, 2009; revised July 7, 2009; accepted July 22, 2009.

This work was supported by grants of the Deutsche Forschungsgemeinschaft (fellowship to N.S.; Center for Molecular Physiology of the Brain, T.M.), the European Community (Eurohear, T.M.), of the Max-Planck-Society (Tandemprojekt, T.M.), Bundesministerium für Bildung und Forschung (Bernstein Center for Computational Neuroscience Göttingen and Bernstein Focus for Neurotechnology, T.M.), and an intramural grant of the University of Göttingen Medical School (A.C.M.). We thank G. Matthews for providing fluorescently labeled CtBP2/RIBEYE-binding peptide, T. Frank for help with Ca²⁺ imaging and providing analysis routines, and T. Frank, A. Neef, A. Lee, D. Oliver, E. Reisinger, and L. Meier for comments on this manuscript. We also thank C. Rüdiger for recordings of ABR and DPOAE and M. Köppler and S. Blume for expert technical assistance. We thank M. McCall and P. Smith for the initial observations that the Ca_v $\beta_2^{-/-}$ mice were deaf. The study was designed by T.M. and R.G.G. The experimental work was performed by J.N. (electrophysiology, Ca²⁺ imaging, immunohistochemistry, and harvesting of IHCs for single-cell PCR), A.G. (ABR; single-unit recordings, which were established, supervised, and coanalyzed by N.S.), A.V.B. (single-cell PCR), and A.C.M. (small contribution at the start of the experiment). R.G.G. provided mice. T.M., J.N., and N.S. prepared this manuscript.

Correspondence should be addressed to either of the following: Tobias Moser, InnerEarLab, Department of Otolaryngology, Göttingen University Medical School, 37099 Göttingen, Germany, E-mail: tmoser@gwdg.de; or Nicola Strenzke, Auditory Systems Physiology Group, Department of Otolaryngology, Göttingen University Medical School, 37099 Göttingen, Germany, E-mail: nicola.strenzke@medizin.uni-goettingen.de.

DOI:10.1523/JNEUROSCI.1577-09.2009

Copyright © 2009 Society for Neuroscience 0270-6474/09/2910730-11\$15.00/0

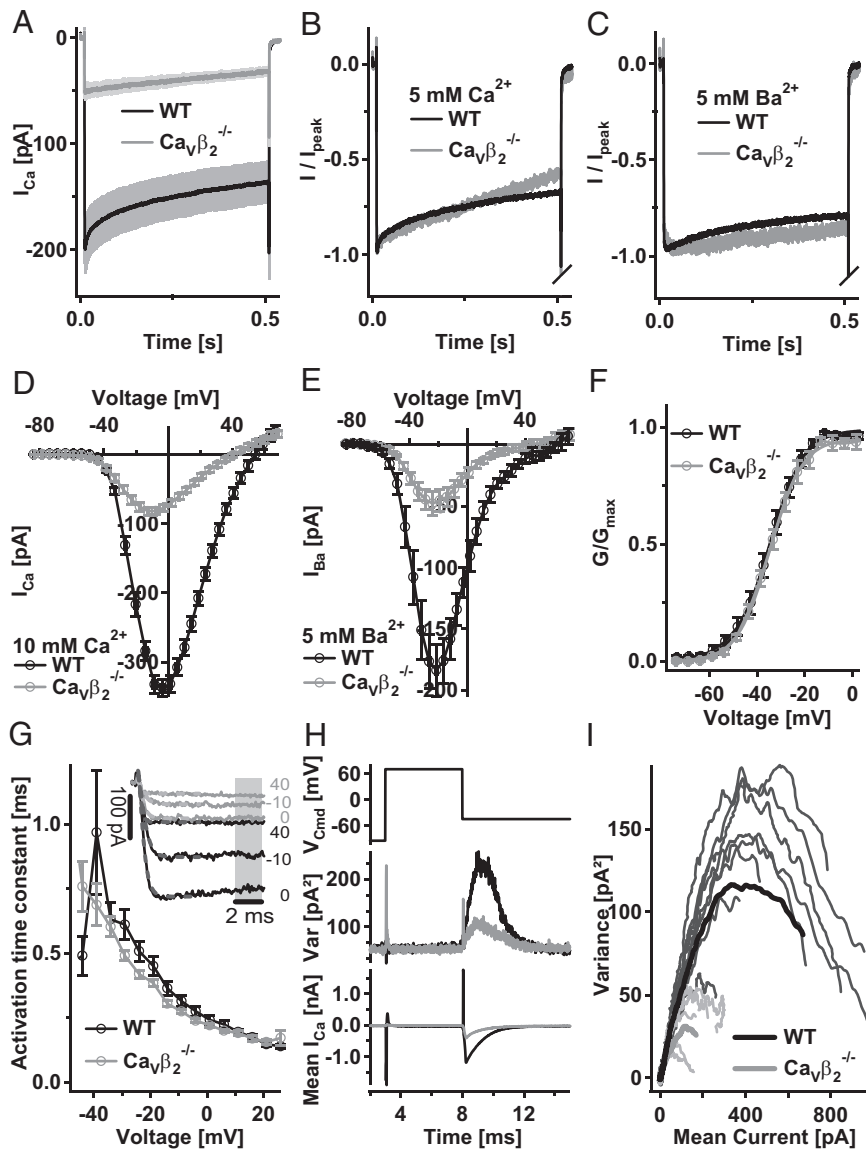


Figure 1. Reduced Ca^{2+} influx in $\text{Ca}_v\beta_2^{-/-}$ IHCs. **A**, Average calcium current ($I_{\text{Ca}} \pm \text{SEM}$) of WT (black \pm light gray; $n = 11$) and $\text{Ca}_v\beta_2^{-/-}$ (gray \pm light gray; $n = 7$) IHCs in response to 500 ms depolarization to -14 mV in 5 mM extracellular Ca^{2+} . **B**, Average I_{Ca} as in **A** but normalized to peak current. Note that calcium current inactivation is enhanced in $\text{Ca}_v\beta_2^{-/-}$ cells but lacks a fast component. **C**, Average currents (normalized to peak) in 5 mM $[\text{Ba}^{2+}]_e$ for WT ($n = 11$) and $\text{Ca}_v\beta_2^{-/-}$ ($n = 7$) IHCs. **D**, Current–voltage (I – V) relationship for WT (black; $n = 8$) and $\text{Ca}_v\beta_2^{-/-}$ (gray; $n = 8$) IHCs in 10 mM $[\text{Ca}^{2+}]_e$. Calcium currents were measured 8 ms after the onset of a depolarization to -14 mV. **E**, I – V relationship, measured as in **D**, with 5 mM $[\text{Ba}^{2+}]_e$ replacing calcium. **F**, Activation curves for Ba^{2+} currents. G/G_{max} curves were calculated with $G = I/(V - V_{\text{reversal}})$ and were fitted individually with a Boltzmann function. The Ba^{2+} reversal potential was linearly extrapolated from the 0–20 mV range in **E**. **G**, Activation time constants of Ca^{2+} currents (same as in **D**) at various membrane voltages were approximated by fitting a power exponential equation,

$$I(t) = I_0 + \Delta I \times (1 - e^{-t/\tau})^2,$$

to the first 5 ms of the current. The inset shows examples of the first 10 ms after depolarization to the potential indicated. The power exponential fits are indicated by dashed lines. The time frame used for building the steady-state I – V in **D** is indicated by the gray bar. **H**, Voltage-clamp protocol (top), variance (middle), and mean calcium current (bottom) calculated from a p/n corrected ensemble of 520 sweeps used to determine the variance–mean plots in **I**. **I**, Calcium current variance versus mean for eight WT (black) and six $\text{Ca}_v\beta_2^{-/-}$ (gray) IHCs. Bold lines represent the overall average.

associated guanylate kinase class of scaffolding proteins (Dolphin, 2003; Hidalgo and Neely, 2007). They bind the α interaction domain of the $\text{Ca}_v\alpha_1$ subunit with high affinity, which is mediated by their α binding pocket (Van Petegem et al., 2004, 2008). $\text{Ca}_v\beta$ subunits are required for plasma membrane traf-

ficking of the $\text{Ca}_v\alpha$ subunit (Bichet et al., 2000), modulate channel gating, and affect the regulation of the channel by G-protein $\beta\gamma$ subunits (for review, see Dolphin, 2003). In addition, they may form part of the physical link between Ca^{2+} channels and the release machinery of docked synaptic vesicles at the presynaptic active zone (Kiyonaka et al., 2007). Thus, $\text{Ca}_v\beta$ subunits could play a role in the establishment of the close colocalization of channel and vesicles that has been suggested to govern stimulus–secretion coupling at the IHC synapse [Ca^{2+} nanodomain control (Brandt et al., 2005; Moser et al., 2006; Goutman and Glowatzki, 2007)].

However, except for the presence of the $\alpha 1D$ subunit (Platzer et al., 2000; Brandt et al., 2003) and Ca^{2+} binding proteins (Yang et al., 2006; Cui et al., 2007), the molecular composition of the hair cell Ca^{2+} channel has not yet been reported. Here, we examined the expression of $\text{Ca}_v\beta$ subunits in IHCs of hearing mice using single IHC reverse transcription (RT)-PCR and found $\text{Ca}_v\beta_2$ to be the predominant $\text{Ca}_v\beta$. To explore the specific role of $\text{Ca}_v\beta_2$ in hearing, we studied viable knock-out mice lacking $\text{Ca}_v\beta_2$ ($\text{Ca}_v\beta_2^{-/-}$) in all but cardiac tissues as a result of heart-specific, transgenic $\text{Ca}_v\beta_2$ expression. These mice show impaired vision, probably attributable to defective synaptic transmission in photoreceptors (Ball et al., 2002). Here we investigated hearing in $\text{Ca}_v\beta_2^{-/-}$ from auditory systems function down to Ca^{2+} channel properties and stimulus–secretion coupling in IHCs.

Materials and Methods

Animals. $\text{Ca}_v\beta_2^{-/-}$ mice with a transgene rescue of cardiac expression (Ball et al., 2002) and C57BL/6 mice were used for experiments between postnatal day 16 (P16) to P21 (single-cell PCR), P21–P28 [hair cell physiology, auditory evoked brainstem responses (ABRs), distortion product otoacoustic emissions (DPOAEs), and immunohistochemistry], and P40–P70 (single auditory neuron recordings). All experiments complied with national animal care guidelines and were approved by the University of Göttingen Board for Animal Welfare and the Animal Welfare Office of the State of Lower Saxony.

Recording of ABRs and DPOAEs. Animals were anesthetized intraperitoneally with a combination of ketamine (125 mg/kg) and xylazine (2.5 mg/kg), and the heart rate was constantly monitored to control the depth of anesthesia. The core temperature was maintained constant at 37°C using a rectal temperature-controlled heat blanket (Hugo Sachs Elektronik–Harvard Apparatus). For stimulus generation, presentation, and data acquisition, we used the TDT II or III Systems (Tucker Davis Technologies) run by BioSig32 software (Tucker Davis Technologies). Sound pressure levels (SPL) are provided in decibels SPL

root mean square (RMS) (tonal stimuli) or decibels SPL peak equivalent (clicks) and were calibrated using a 1/4 inch Brüel and Kjær microphone (model 4939). Tone bursts (4/8/12/16/24/32 kHz, 10 ms plateau, 1 ms \cos^2 rise/fall) or clicks of 0.03 ms were presented at 20 Hz in the free field ipsilaterally using a JBL 2402 speaker. The difference potential between vertex and mastoid subdermal needles was amplified (50,000 times), filtered (low pass, 4 kHz; high pass, 100 Hz) and sampled at a rate of 50 kHz for 20 ms, 2×2000 times to obtain two mean ABRs for each sound intensity. Hearing threshold was determined with 10 dB precision as the lowest stimulus intensity that evoked a reproducible response waveform in both traces by visual inspection. For DPOAEs, a 24-bit sound card and the ED1/EC1 speaker system (Tucker David Technologies) were used to generate two primary tones (f_2/f_1 ratio: 1.2). Primary tones were coupled into the ear canal by a custom-made probe containing an MKE-2 microphone (Sennheiser) and adjusted to an intensity of 60 dB sound pressure level at the position of the ear drum as mimicked in a mouse ear coupler. The microphone signal was amplified (DMP3; Midiman) and analyzed by fast Fourier transformation.

Recordings from single-unit auditory nerve fibers. Auditory nerve fiber recordings were performed essentially as described by Taberner and Liberman (2005) and Strenzke et al. (2009), using the TDT System 3 and an ELC-03XS amplifier (NPI Electronics) controlled by Matlab software (MathWorks) and using free-field stimulation with a JBL 2402 speaker. Mice aged 6–10 weeks were anesthetized with urethane (1.3 mg/kg, i.p.) and xylazine (5 mg/kg i.p.), tracheotomized, and placed in a stereotaxic apparatus. After partial removal of the left occipital bone and cerebellum, the auditory nerve was approached through the cochlear nucleus with a glass micropipette filled with 3 M NaCl and 2% methylene blue using an Inchworm manipulator (EXFO Burleigh). During audiovisual detection of single-unit spiking activity, auditory nerve fibers were identified by their stereotaxic position, irregular firing pattern, and their primary-like poststimulus time histogram (PSTH). A description of units with different discharge properties is provided in supplemental Figure 4 (available at www.jneurosci.org as supplemental material). Characteristic frequency (CF) and best threshold (defined by a significant rate increase by 20 spikes/s within 20 ms from the start of a 15 ms tone pip, Wald's probability ratio test) were obtained with a $1/32$ octave and 2 dB precision, and additional characterization was performed at CF. In fibers with poor frequency tuning, individual best frequencies were chosen manually during audiovisual cues or systematic scanning of the receptive field. For subsequent offline spike detection using custom-written Matlab routines, recorded traces were matched to a spike template that was generated for each unit based on a manually set spike threshold value. The success of this procedure was confirmed by inspection of sorted waveforms.

Patch-clamp and confocal Ca^{2+} imaging. IHCs from apical coils of freshly dissected organs of Corti were patch clamped as described previously (Moser and Beutner, 2000). For recordings of Ca^{2+} current and exocytosis, the pipette solution contained the following: 130 mM Cs-gluconate, 10 mM tetraethylammonium (TEA)-Cl, 10 mM 4-AP, 10 mM HEPES, 1 mM $MgCl_2$, 2 mM EGTA (for Ca^{2+} imaging), 0.4 mM Fluo-5N (for Ca^{2+} imaging), and 250 μ g/ml amphotericin B (for perforated-patch recordings), pH 7.2. For whole-cell recordings, 2 mM Mg-ATP and 0.3 mM Na-GTP were added to the solution. The extracellular solution contained the following (in mM): 99 NaCl, 35 TEA-Cl, 2.8 KCl, 2, 5, or 10 $CaCl_2$, 0.005 BayK8644 (for fluctuation analysis), 0.1 apamin, 1 $MgCl_2$, 5 4-AP, 1 CsCl, 10 HEPES, and 10 D-glucose, pH 7.2. For lower Ca^{2+} concentrations, $CaCl_2$ was replaced by equimolar amounts of NaCl. K^+ currents were recorded with intracellular solution containing the following (in mM): 150 KCl, 1 $MgCl_2$, 10 HEPES, 2 Mg-ATP, and 0.3 Na-GTP. The extracellular solution contained the following (in mM): 144 NaCl, 5.8 KCl, 1 $MgCl_2$, 2 $CaCl_2$, 10 HEPES, and 10 D-glucose. EPC-9 amplifiers (HEKA) controlled by Pulse or Patchmaster software (HEKA) were used for measurements. All voltages were corrected for liquid junction potentials. Currents were leak corrected using a p/10 protocol. For measurements of K^+ currents, the series resistance (R_s) compensation of the Pulse software was used to compensate 70% of the R_s during the experiments. The remaining voltage error caused by residual R_s was corrected offline according to $U_{error} = R_{s,residual} \times I_{steady-state}$.

Table 1. Number of channels, single-channel current, and maximum open probability as obtained by nonstationary fluctuation analysis

	WT	$Ca_v\beta_2^{-/-}$	p value
Number of channels N	1298 ± 100	596 ± 98	$p < 0.001^{***}$
Single channel current i (pA)	0.59 ± 0.06	0.48 ± 0.03	$p = 0.128$
Maximum open probability p	0.82 ± 0.06	0.69 ± 0.09	$p = 0.233$

Data were acquired from parabolic fits to variance versus mean traces from WT ($n = 9$) and $Ca_v\beta_2^{-/-}$ ($n = 6$) as shown in Figure 1H. Values are expressed as mean \pm SEM and were compared using Student's unpaired t test.

Variance of Ca^{2+} tail currents recorded at -64 mV was estimated as the average of squared differences between pairs of consecutive responses, as described previously (Roberts et al., 1990; Brandt et al., 2005), to minimize effects of Ca^{2+} current rundown. Variance was plotted against the mean current I_{mean} , and fitting according to the following:

$$var = i \times I_{mean} - \frac{I_{mean}^2}{N} + \text{Offset} \quad (1)$$

was used to estimate N (the total number of Ca^{2+} channels) and i (the single channel current). Data were only taken into account starting 600 μ s after repolarization, and curve fitting disregarded another 10 points (see Fig. 3H, rightmost) to avoid impact of residual capacitive currents. The maximum open probability (P_o) was then derived from

$$P_o = \frac{I_{mean,max}}{N \times i} \quad (2)$$

For capacitance measurements, IHCs were stimulated by depolarizations of different durations to -14 mV at intervals of 30 to 60 s. We measured membrane capacitance increments (ΔC_m) as described previously (Moser and Beutner, 2000), averaging 400 ms before and after (skipping the first 40 ms) the depolarization. Mean ΔC_m and Ca^{2+} current estimates present grand averages calculated from the mean estimates of individual IHCs. This avoided dominance of IHCs contributing more sweeps.

For Ca^{2+} imaging, an Olympus Fluoview 300 confocal scanner (R3896 P.M.T., Hamamatsu, as detector) mounted to a BX50WI microscope (0.9 numerical aperture, 60 \times water-immersion objective; Olympus) and a 50 mW, 488 nm solid state laser (Cyan; Newport-Spectraphysics) were used. Ca^{2+} microdomain overview images were acquired as background-subtracted averages of 1296×96 pixel images acquired during six consecutive 390 ms depolarizations to -14 mV. During spot detection ("point scan"), we attenuated the laser light to 0.05% of maximum intensity and read out the photomultiplier signal at 500 kHz, followed by temporal averaging to yield an effective rate of 2 kHz. To quantify the onset kinetics of microdomains, point scan data were fitted with a single- or double-exponential function when appropriate. For statistics of the onset kinetics, we pooled the time constants of single-exponential fits with those of the fast component of double-exponential fits. Analysis of electrophysiology and imaging data was performed in Igor Pro software (Wavemetrics). Means were expressed \pm SEM and compared using Student's unpaired t tests, with $*p < 0.05$, $**p < 0.01$, and $***p < 0.001$, respectively.

Single IHC RT-PCR. Single IHC RT-PCR can be found in supplemental Figure 1 and supplemental Table 1, available at www.jneurosci.org as supplemental material.

Immunohistochemistry and confocal microscopy of immunolabeled hair cells. The freshly dissected apical cochlear turns were fixed with 4% formaldehyde in PBS for 1 h on ice or with methanol for 20 min at -20°C . Thereafter, the tissue was washed three times for 10 min in PBS and incubated for 1 h in goat serum dilution buffer (GSDB) (16% normal goat serum, 450 mM NaCl, 0.3% Triton X-100, and 20 mM phosphate buffer, pH 7.4) in a wet chamber at room temperature. Primary antibodies were dissolved in GSDB and applied overnight at $+4^\circ\text{C}$ in a wet chamber. After washing three times for 10 min (wash buffer: 450 mM NaCl, 20 mM phosphate buffer, and 0.3% Triton X-100), the tissue was incubated with secondary antibodies in GSDB in a wet light-protected chamber for 1 h at room temperature. Then the preparations were washed three times for 10 min in wash buffer and one time for 10 min

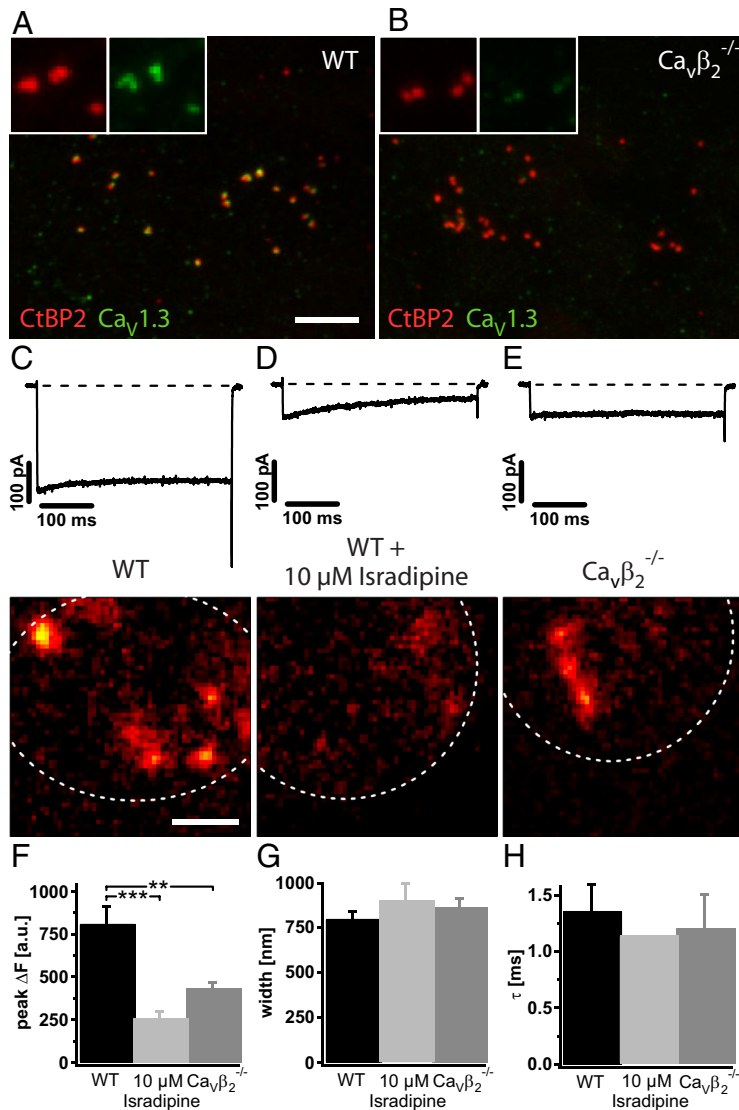


Figure 2. Clustering of fewer Ca^{2+} channels at the synapses of $Ca_v\beta_2^{-/-}$ IHCs. **A, B**, Representative projections of confocal sections from WT (**A**) and $Ca_v\beta_2^{-/-}$ (**B**) IHCs immunolabeled for ribbons (anti-CtBP2) and the $Ca_v1.3$ channels (anti- $\alpha 1D$). In WT, there is clear overlap (yellow) indicating colocalization of Ca^{2+} channel clusters and ribbons. Scale bar, 5 μm . Insets show separated color channels in a higher magnification (field of view, $3.27 \times 3.27 \mu m$). **C–E**, Representative Ca^{2+} current traces in WT IHCs (in response to 390 ms depolarizations to -14 mV) in the absence (**C**) and presence (**D**) of 10 μM of the Ca-channel-blocker isradipine and in a $Ca_v\beta_2^{-/-}$ IHC (**E**). Below, background-subtracted confocal scans of the corresponding cells (outlined) filled with the fluorescent calcium indicator Fluo-5N (400 μM) and calcium chelator EGTA (2 mM) through a patch pipette are shown during depolarization. Scale bar, 2 μm [identical color scaling in **C–E**, ranging from 0 (black) to 805 (yellow)]. Hotspots of calcium entry can be recognized in WT and $Ca_v\beta_2^{-/-}$ IHCs. **F**, Average peak fluorescence of Ca^{2+} microdomains derived from Gaussian fits to line profiles of individual hotspots (background subtracted). The difference between WT ($n = 24$ Ca^{2+} microdomains from 6 IHCs) and isradipine-blocked WT ($n = 11$ Ca^{2+} microdomains from 4 IHCs) hotspots is significant at $p < 0.001$, and that between WT and $Ca_v\beta_2^{-/-}$ ($n = 23$ Ca^{2+} microdomains from 7 IHCs) is significant at $p < 0.01$. **G**, Average full-width at half-maximum derived from the same Gaussian fits as in **F**. **H**, Average (fast) activation time constants of fluorescence increase derived from high temporal resolution point scans of individual Ca^{2+} microdomains ($n = 17$ Ca^{2+} microdomains from 8 WT IHCs, 2 Ca^{2+} microdomains from 2 isradipine-treated WT IHCs, and 9 Ca^{2+} microdomains from 5 $Ca_v\beta_2^{-/-}$ IHCs).

in 5 mM phosphate buffer, placed onto the glass microscope slides with a drop of fluorescence mounting medium (Dako), and covered with thin glass coverslips. The following antibodies were used: mouse IgG1 anti-CtBP2 (also recognizing the ribbon protein RIBEYE; 1:150; BD Biosciences), rabbit anti- $\alpha 1D$ (1:75; Alomone Labs), rabbit anti-large-conductance Ca^{2+} activated K^+ channels (BK channels) (1:200; Sigma), mouse anti-synaptophysin (1:200; Synaptic Systems), rabbit anti-small conductance Ca^{2+} activated K^+ channels (SK2 channels) (1:200; Sigma), rabbit anti-GluR 2/3 (1:200; Millipore Bioscience Research Reagents), mouse anti-parvalbumin 235 (1:500; Swant), and

secondary AlexaFluor488- and AlexaFluor568-labeled antibodies (1:200; Invitrogen). Confocal images were acquired using a laser scanning confocal microscope (Leica TCS SP5) with 488 nm (argon) and 561 nm (helium–neon) lasers for excitation and a 63 \times oil-immersion objective (1.4 numerical aperture; Leica). Whole-mount preparations of the organ of Corti provided the possibility to analyze several IHCs in a row (Khimich et al., 2005). Images were processed using NIH ImageJ and assembled for display in Adobe Illustrator software (Adobe Systems).

Electron microscopy. The organs of Corti were fixed immediately after dissection with 2.5% glutaraldehyde for 20 min at room temperature in HEPES–HBSS containing the following: 5.36 mM KCl, 141.7 mM NaCl, 1 mM $MgCl_2$, 0.5 mM $MgSO_4$, 10 mM HEPES, 0.1 mg/ml L-glutamin, and 2 mg/ml glucose. The pH was adjusted to 7.2. Thereafter, the samples were fixed overnight at 4°C in 2.5% glutaraldehyde in 0.1 M cacodylic buffer at pH 7.4. After an additional fixation in 0.1% OsO_4 , the samples were stained with 1% uranyl acetate and dehydrated in a series of EtOH and finally in propylene oxide. They were then embedded in Agar 100 (purchased through Science Services). Thin sections (80 nm) were counterstained with lead citrate and examined using a Philips CM 120 BioTwin transmission electron microscope (Philips). Pictures were taken with a TemCam F224A camera (TVIPS) at 20,000-fold magnification.

Results

$Ca_v\beta_2$ is abundant in IHCs and critical for IHC Ca^{2+} influx

First, we tested expression of the four known $Ca_v\beta$ s in IHCs by RT-PCR. We found expression of $Ca_v\beta_{1-4}$ in the cochlea (our unpublished data). Next, we harvested mRNA from single IHCs, subjected it to reverse transcription, and performed a multiplex PCR for preamplification of all isoforms, followed by an isoform-specific nested PCR (supplemental Fig. 1, available at www.jneurosci.org as supplemental material). Otoferlin, a hair-cell-specific marker (Roux et al., 2006), was used as positive control. $Ca_v\beta_2$ mRNA was found in 14 of 16 wild-type (WT) IHCs but not in $Ca_v\beta_2^{-/-}$ IHCs ($n = 16$ otoferlin-positive IHC from two mice each for WT and $Ca_v\beta_2^{-/-}$). In few WT and $Ca_v\beta_2^{-/-}$ IHCs, we also detected mRNA for $Ca_v\beta_1$ (WT, 1 of 16; $Ca_v\beta_2^{-/-}$, 2 of 16) and $Ca_v\beta_3$ (WT, 4 of 16; $Ca_v\beta_2^{-/-}$, 0 of 16) but not for $Ca_v\beta_4$. In conclusion, although the single-cell PCR data do not allow for quantification of mRNA levels, the prevalent detection of $Ca_v\beta_2$ mRNA compared with the scarce identification of other $Ca_v\beta$ mRNAs indicates that $Ca_v\beta_2$ mRNA is the most abundant $Ca_v\beta$ transcript in IHCs.

Ca^{2+} currents of 3- to 4-week-old $Ca_v\beta_2^{-/-}$ mice were drastically reduced at all potentials tested (by $\sim 70\%$) (Fig. 1A,D). The remaining Ca^{2+} current showed a comparable voltage de-

pendence (Fig. 1D) and was mostly mediated by L-type channels because it was augmented by the dihydropyridine agonist BayK8644 like that observed in WT IHCs (172% $Ca_v\beta_2^{-/-}$ vs 160% WT) (supplemental Fig. 2C,D, available at www.jneurosci.org as supplemental material). By replacing external Ca^{2+} with Ba^{2+} , we could study voltage-dependent inactivation in isolation from Ca^{2+} -dependent inactivation (CDI). CDI was clearly altered in $Ca_v\beta_2$ -deficient IHCs: it lacked the fast component and displayed an accelerated slow component (Fig. 1A,B). Approximation of the slow component by fitting of a linear function to the last 250 ms of the normalized current resulted in an average slope of $0.275 \pm 0.042 s^{-1}$ for WT and $0.663 \pm 0.047 s^{-1}$ for $Ca_v\beta_2^{-/-}$ IHCs (the difference is significant at $p < 0.001$). Voltage-dependent inactivation, however, was unaltered in $Ca_v\beta_2^{-/-}$ IHCs (average line slope of $0.167 \pm 0.026 s^{-1}$ for WT and $0.218 \pm 0.054 s^{-1}$ for $Ca_v\beta_2^{-/-}$; $p = 0.413$) (Fig. 1C).

Voltage dependence of $Ca_v1.3$ channel activation was studied using Ba^{2+} as the permeating ion to maximally inhibit contaminating potassium currents, which could compromise the analysis. Ba^{2+} currents of $Ca_v\beta_2^{-/-}$ and control IHCs showed indistinguishable potentials for half-maximal activation ($Ca_v\beta_2^{-/-}$ IHCs, $V_{1/2} = 21.0 \pm 4.2$ mV and WT IHCs, $V_{1/2} = -20.6 \pm 3.0$ mV) (Fig. 1E,F). The time constant of Ca^{2+} current activation was essentially unchanged, except for a slight shift toward more negative potentials in $Ca_v\beta_2^{-/-}$ IHCs (Fig. 1G).

To explore the mechanism underlying the Ca^{2+} current reduction, we performed a nonstationary fluctuation analysis on Ca^{2+} tail currents in the presence of BayK8644 (Roberts et al., 1990; Brandt et al., 2005). Figure 1H shows representative examples of ensemble variance and mean (for details, see Materials and Methods). Both variance and mean were strongly reduced in $Ca_v\beta_2^{-/-}$ IHCs (Fig. 1I). The analysis indicated an $\sim 60\%$ decrease in the number of functional channels but comparable single-channel currents and maximal open probabilities (Table 1). The notion of a reduced surface expression of $Ca_v1.3$ channels was corroborated by immunohistochemistry (Fig. 2A,B). $\alpha 1D$ immunofluorescent spots colocalizing with synaptic ribbons (stained for RIBEYE/CtBP2) (Khimich et al., 2005) were observed in WT IHCs. After identical tissue processing and imaging, we found very sparse if any $\alpha 1D$ immunofluorescence at the ribbons of $Ca_v\beta_2^{-/-}$ IHCs (Fig. 2A,B, insets). Unfortunately, the anti- $\alpha 1D$ antibody caused considerable unspecific stain-

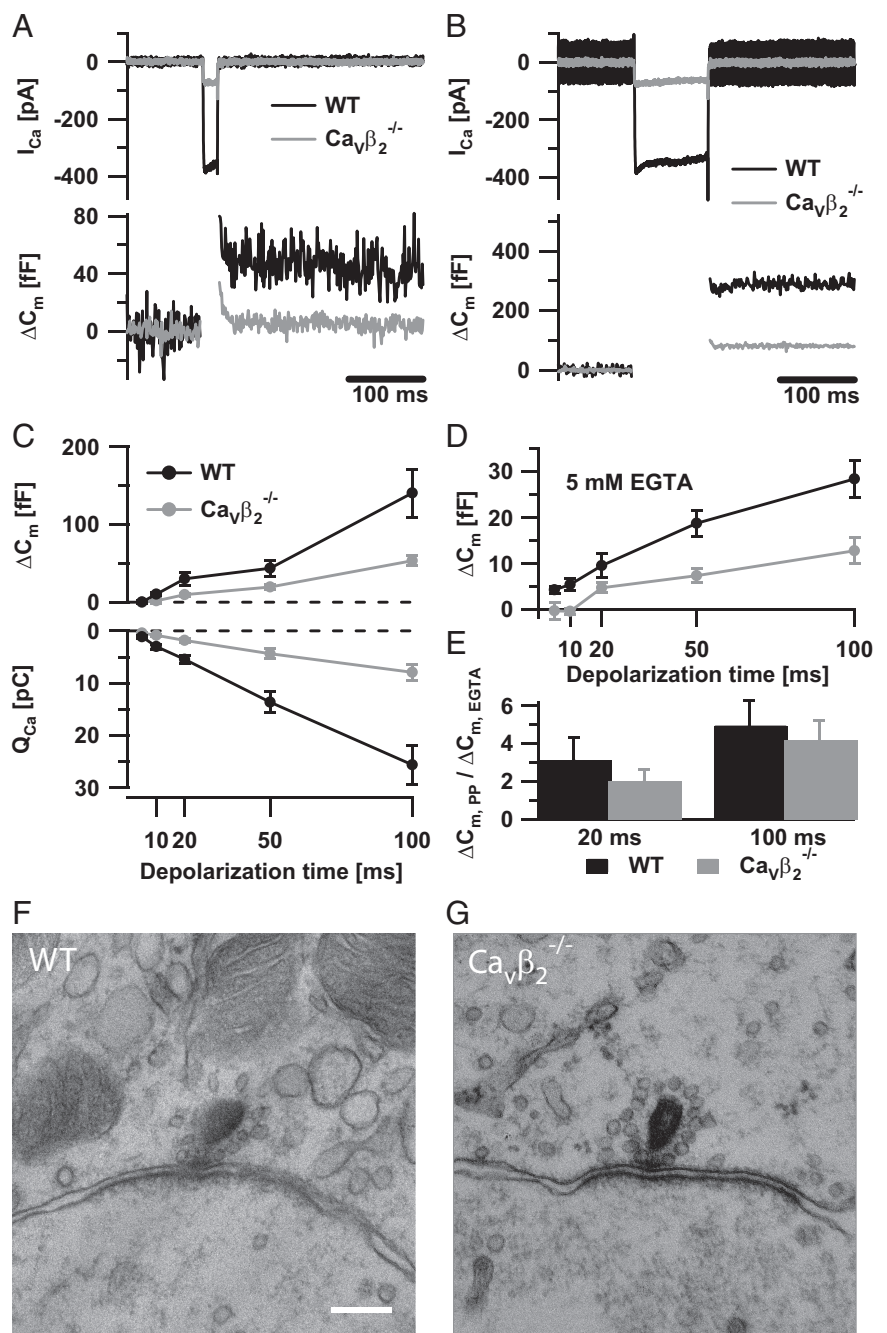


Figure 3. Reduced exocytosis but maintained Ca^{2+} influx–exocytosis coupling. **A, B**, Representative Ca^{2+} currents and membrane capacitance changes (ΔC_m) elicited by depolarizations to -14 mV for 20 ms (**A**) and 100 ms (**B**) in WT (black) and $Ca_v\beta_2^{-/-}$ (gray) IHCs. The extracellular solution contained 10 mM $[Ca^{2+}]$, and recordings were done in perforated-patch configuration. **C**, Average ΔC_m and Q_{Ca} for various depolarization (-14 mV) durations in WT (black; $n = 7$) and $Ca_v\beta_2^{-/-}$ (gray; $n = 8$) IHCs obtained in the perforated-patch configuration. **D**, Average ΔC_m for various depolarization durations in WT (black; $n = 9$) and $Ca_v\beta_2^{-/-}$ (gray; $n = 7$) IHCs in standard whole-cell configuration with 5 mM EGTA in the pipette solution. **E**, Ratio of exocytosis between perforated-patch ($\Delta C_{m,pp}$, endogenous buffer) and ruptured-patch ($\Delta C_{m,EGTA}$, 5 mM EGTA) configuration for WT and $Ca_v\beta_2^{-/-}$ IHCs for 20- and 100-ms-long depolarizations. The relative errors (SEM/mean) were propagated from the errors (SEM) of the mean responses in perforated-patch and ruptured-patch (5 mM EGTA) experiments. **F, G**, Electron micrographs of synaptic ribbons in WT (**F**) and $Ca_v\beta_2^{-/-}$ (**G**) IHCs. Scale bar, 200 nm.

ing [evident also in IHCs of $\alpha 1D^{-/-}$ mice (Brandt et al., 2005)]. Therefore, we favor the interpretation that $\alpha 1D$ immunofluorescence outside ribbon-type active zones reflects unspecific labeling rather than mislocalized channels. The number of ribbon synapses per IHC (estimated by relating the numbers of ribbons and IHC nuclei in one stack of confocal

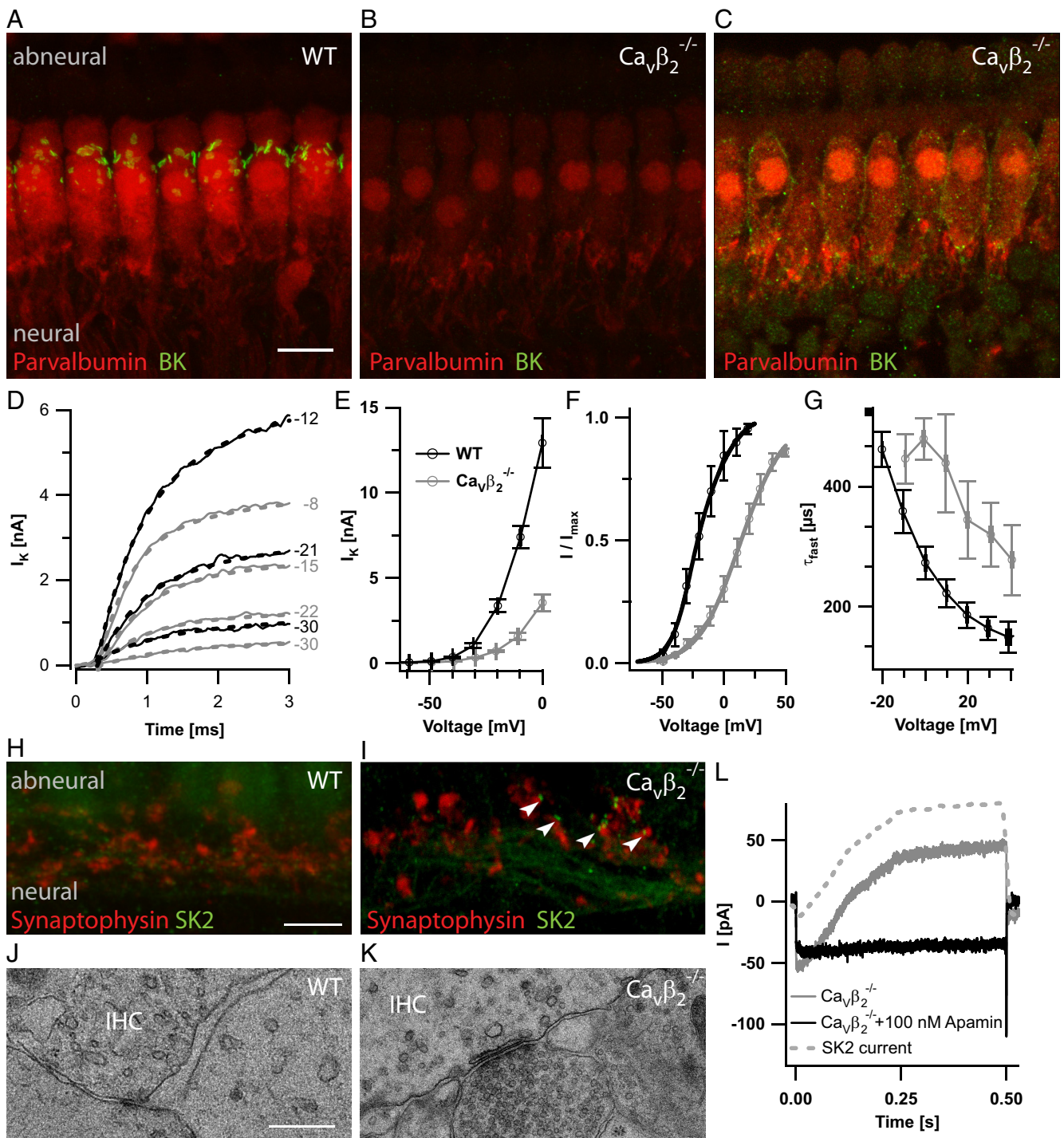


Figure 4. Impaired IHC development in $Ca_v\beta_2^{-/-}$ IHCs. **A, B**, Projection of confocal sections of representative WT (**A**) and $Ca_v\beta_2^{-/-}$ (**B**) organs of Corti immunostained for BK channels (green) and parvalbumin (red). Tissue was processed identically, and images were acquired under identical conditions. Clusters of BK channels are found at the neck of WT IHCs but not in $Ca_v\beta_2^{-/-}$ IHCs. Scale bar, 10 μ m. **C**, Single confocal section from data in **B** imaged with a higher overall exposure reveals faint BK immunofluorescence along the entire IHC membrane, which was not observed in WT animals. **D**, The first 3 ms of potassium current in response to 100 ms step depolarizations to the potentials indicated (in millivolts) from a representative WT (black) and $Ca_v\beta_2^{-/-}$ (gray) IHC, overlaid with the double-exponential fits to the currents (dashed lines), which revealed the activation time constants shown in **G**. **E**, Steady-state $I-V$ relationship of K^+ currents for WT (black; $n = 20$) and $Ca_v\beta_2^{-/-}$ (gray; $n = 5$) IHCs obtained from averaging the current during the last 0.5 ms of 3-ms-long depolarizations. **F**, Average fractional activation curves acquired from measuring the tail currents between 0.2 and 0.3 ms after the end of a 3 ms depolarizing test pulse (data as in **E**). Markers represent average data, and continuous lines are the averaged fits to the following equation:

$$I = \frac{I_{max}}{1 + \exp\left(\frac{V_{1/2} - V}{slope}\right)}$$

Average values \pm SEM for the fit coefficients are as follows: $V_{1/2}$, -22.85 ± 4.27 mV for WT and 10.80 ± 4.04 mV for $Ca_v\beta_2^{-/-}$; slope, 8.7 ± 0.1 mV for WT and 1.5 ± 0.7 mV for $Ca_v\beta_2^{-/-}$. The differences are significant at $p < 0.001$. **G**, Average fast activation time constants of the K^+ current obtained by fitting a double-exponential function to the first 20 ms of 100 ms depolarization pulses to the potentials indicated. **H, I**, Immunostainings for SK2 channels (green) and synaptophysin (red) of the basal region of IHC from a WT (**G**, P21) and a $Ca_v\beta_2^{-/-}$ mouse (**H**, P23). The green background staining arises from pillar cells, which often show unspecific immunoreactivity. Note, however, the presence of SK2-positive spot-like structures in $Ca_v\beta_2^{-/-}$ IHCs (arrowheads), which can be seen in most, but not all cells and which are absent from mature WT cells. Scale bar, 5 μ m. **J, K**, Electron micrographs of the basal IHC plasma membrane (Figure legend continues.)

sections) was unaltered in $Ca_v\beta_2^{-/-}$ IHCs [11.3 ± 0.3 ($n = 37$ IHCs, 3 mice) vs 11.5 ± 0.3 in WT ($n = 40$ IHCs, 5 mice) at 4 weeks of age]. Together, the data suggest a defective surface expression of $Ca_v1.3$ channels in the absence of $Ca_v\beta_2$, consistent with a critical role of this $Ca_v\beta$ isoform for $\alpha 1D$ membrane trafficking/stabilization at the membrane in IHCs.

Ca²⁺ channels still cluster at presynaptic active zones in $Ca_v\beta_2^{-/-}$ IHCs

The faint $\alpha 1D$ immunofluorescence observed at the ribbons of $Ca_v\beta_2^{-/-}$ IHCs suggested that the preferential synaptic localization was at least partially preserved for the remaining $Ca_v1.3$ channels. To test this more rigorously, we performed confocal Ca^{2+} imaging in IHCs of 3- to 4-week-old $Ca_v\beta_2^{-/-}$ and WT mice using the low-affinity Ca^{2+} indicator Fluo-5N ($K_D = 90 \mu M$). Depolarization revealed fluorescence hotspots in WT IHCs (Fig. 2C), which resemble presynaptic Ca^{2+} microdomains building up during voltage-gated Ca^{2+} influx at the active zones of the IHC (Frank et al., 2009). To test whether Ca^{2+} influx as small as that observed in $Ca_v\beta_2^{-/-}$ IHCs could be expected to cause detectable Ca^{2+} microdomains, we reduced the Ca^{2+} influx of WT IHCs to $\sim 25\%$ by dihydropyridine block (isradipine, $10 \mu M$). Indeed, we observed Ca^{2+} microdomains in dihydropyridine-treated wild-type IHCs (Fig. 2D) and in untreated $Ca_v\beta_2^{-/-}$ IHCs (Fig. 2E). In both conditions, we found reduced amplitudes (Fig. 2F) but no obvious changes of their spatiotemporal properties (Fig. 2G,H). When labeling the synaptic ribbon with a RIBEYE-binding peptide (Zenisek et al., 2004; Frank et al., 2009), depolarization-induced Ca^{2+} hotspots were observed at the positions of almost all labeled ribbons (28 hotspots at 30 labeled ribbons for WT, 11 hotspots at 13 labeled ribbons for $Ca_v\beta_2^{-/-}$) (for examples, see supplemental Fig. 3, available at www.jneurosci.org as supplemental material).

Major reduction of exocytosis in $Ca_v\beta_2^{-/-}$ mice

Exocytosis elicited by strong step depolarizations (to -14 mV) was monitored as changes in membrane capacitance. Depolarization-evoked exocytosis was substantially reduced in $Ca_v\beta_2^{-/-}$ IHCs (Fig. 3). To enhance exocytosis, we performed the experiments at an elevated extracellular Ca^{2+} concentration (10 mM $[Ca^{2+}]_e$), but comparable results were obtained at 2 mM $[Ca^{2+}]_e$ (supplemental Fig. 2A,B, available at www.jneurosci.org as supplemental material). Fast and sustained components of exocytosis were similarly affected, and their decrease [68% for 20 ms depolarizations primarily recruiting the readily releasable pool (RRP); 62% for 100 ms depolarizations recruiting RRP and sustained exocytosis] was comparable with that of the Ca^{2+} influx (20 ms, 67%; 100 ms, 68%) in these perforated-patch recordings (Fig. 3A–C).

Next, we probed the spatial coupling of Ca^{2+} influx and exocytosis in whole-cell experiments by adding 5 mM of the “slow” Ca^{2+} chelator EGTA to the pipette solution. The rationale of the experiment was to test for the potency of EGTA in competing

with the Ca^{2+} sensor of the release machinery for Ca^{2+} binding. EGTA suppressed exocytosis in WT and $Ca_v\beta_2^{-/-}$ IHCs (Fig. 3D). The relative reduction of exocytosis in whole-cell experiments (with high [EGTA]) versus perforated-patch experiments (with endogenous buffers) was comparable between WT and $Ca_v\beta_2^{-/-}$ IHCs (Fig. 3E). The low sensitivity of exocytosis to Ca^{2+} buffering by millimolar EGTA suggests that the remaining Ca^{2+} channels were as tightly coupled to release ready vesicles in $Ca_v\beta_2^{-/-}$ IHCs as in normal IHCs. Electron micrographs of ribbon synapses also did not show gross alterations of synapse ultrastructure in $Ca_v\beta_2^{-/-}$ mice (Fig. 3F,G).

Impaired postnatal hair cell development in $Ca_v\beta_2^{-/-}$ mice

IHCs pass through a postnatal differentiation period refining Ca^{2+} signaling, afferent synapse number, and morphology, acquiring mature potassium channel expression and mostly losing efferent innervation (Kros et al., 1998; Beutner and Moser, 2001; Marcotti et al., 2003; Katz et al., 2004). This postnatal differentiation depends on thyroid hormone signaling (Brandt et al., 2007; Sendin et al., 2007) and probably on active IHC Ca^{2+} signaling (Brandt et al., 2003; Nemzou et al., 2006). In analogy to the findings in $\alpha 1D^{-/-}$ mice (Brandt et al., 2003; Nemzou et al., 2006), we anticipated an impaired IHC development of $Ca_v\beta_2^{-/-}$ mice.

Immunolabeling revealed clusters of large conductance voltage and BK channels at the “neck” of normal IHCs after the onset of hearing (Fig. 4A, $n = 4$ cochleae) (Pyott et al., 2004; Hafidi et al., 2005; Nemzou et al., 2006). In contrast, $Ca_v\beta_2^{-/-}$ IHCs lacked spot-like immunofluorescence even at 4 weeks after birth (Fig. 4B,C, $n = 4$ cochleae). However, they showed a weak and diffuse BK immunofluorescence at the IHC membrane when examined with increased excitation intensity and detection sensitivity (Fig. 4C), which was not observed in WT IHCs with the same microscope settings (our unpublished data). Rapidly activating outward currents, reminiscent of BK currents, were observed also in $Ca_v\beta_2^{-/-}$ IHCs of 3–4 weeks of age (Fig. 4D). However, they showed reduced amplitudes and a depolarized shift of activation (Fig. 4E–G). $Ca_v\beta_2^{-/-}$ IHCs displayed a $\sim 75\%$ reduction in outward current when measured at the end of 3-ms-long depolarizations [mostly recruiting BK channels (Kros and Crawford, 1990)] in the range of -84 to -4 mV. The difference of the average current (-8 ± 2.57 nA at -4 mV) was similar to that measured at the end of a 100 ms depolarizing pulse (-11 ± 1.9 nA at -4 mV) (our unpublished data), suggesting that the knock-out rather selectively affected the BK current but left the other potassium currents unchanged. The $V_{1/2}$, obtained from analysis of tail currents after 3 ms depolarizations, was, on average, shifted by 32 mV in depolarizing direction. In addition, the average slope factor (s) was decreased by 6.3, indicating a shallower voltage dependence. Although there was a comparable kinetics of activation at the respective $V_{1/2}$, the activation time constant of $Ca_v\beta_2^{-/-}$ IHCs did not approximate the asymptotic value of the WT cells even at the most depolarized potentials achieved (e.g., $p < 0.05$ for WT at 10 mV vs $Ca_v\beta_2^{-/-}$ at 40 mV) (Fig. 4G).

As an additional sign of impaired postnatal IHC differentiation, a number of $Ca_v\beta_2^{-/-}$ IHCs showed colocalized immunofluorescence of synaptophysin and SK2 channels, respectively, at 4 weeks after birth (Fig. 4H,I, $n = 2$ cochleae). This indicates the persistence of the developmental efferent IHC innervation, which is normally lost after the onset of hearing (Katz et al., 2004) and hence was not found in IHCs of 4-week-old WT mice (Fig. 4H). Electron micrographs also revealed multiple efferent synapses onto IHCs of $Ca_v\beta_2^{-/-}$ mice (for an example, see Fig. 4K),

←

(Figure legend continued.) from WT (J) and $Ca_v\beta_2^{-/-}$ (K) mice. The IHC label indicates the cytoplasm of the hair cell. Note the vesicle-filled terminals of efferent fibers making contact with the IHC (J; seen in $n = 2$ cochleae), which were frequently encountered in $Ca_v\beta_2^{-/-}$ mice but rarely in WT animals (K; $n = 2$ cochleae). Scale bar, 500 nm. L, Apamin-sensitive current in a representative recording from a $Ca_v\beta_2^{-/-}$ IHC in response to a 500 ms depolarization pulse to -14 mV (Ca^{2+} -based pipette solution, extracellular solution containing 5 mM Ca^{2+}): current before (gray) and after (black) addition of 100 nM apamin as well as difference current (dotted line). The small inward component in the difference current reflects Ca^{2+} current rundown during the wash-in of apamin.

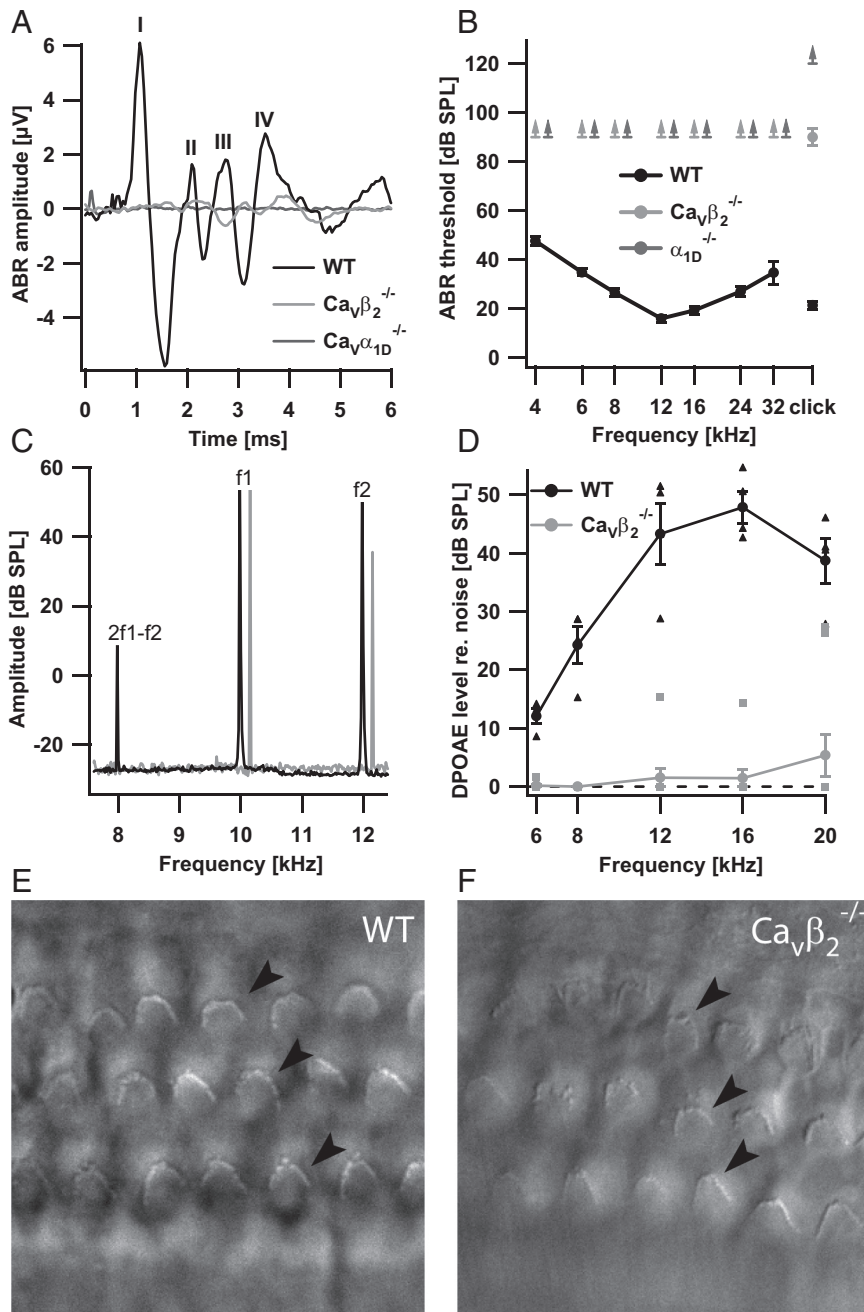


Figure 5. $Ca_v\beta_2^{-/-}$ mice are profoundly hearing impaired. **A**, Grand average of ABRs elicited by suprathreshold click stimuli (100 dB peak equivalent) in WT (black; $n = 9$) and $Ca_v\beta_2^{-/-}$ (light gray; $n = 5$) mice. For comparison, the ABR from $\alpha 1D^{-/-}$ mice (dark gray; $n = 2$) is shown, which lacks a detectable response to 100 dB clicks. **B**, Hearing thresholds obtained by ABR recordings. The average threshold of $Ca_v\beta_2^{-/-}$ (light gray; $n = 5$ mice) amounts to 90 dB for clicks and exceeds 90 dB (SPL RMS, the highest sound pressure level tested) for 4–32 kHz tone bursts. For comparison, the mean audiograms of WT (black; $n = 9$) and $\alpha 1D^{-/-}$ (dark gray; $n = 2$, no detectable responses to clicks even at 120 dB SPL) mice are shown. **C**, Representative power spectrum of microphone signal showing primary tones (f1 and f2, 60 dB SPL) and DPOAE at 2f1 – f2 in the WT mouse (black). The trace of the $Ca_v\beta_2^{-/-}$ mouse (gray) is laterally offset by 150 Hz for better readability and shows no detectable DPOAE. **D**, Grand averages of DPOAE levels (relative to the noise floor): sizable DPOAE across all tested frequencies in WT mice (black; $n = 4$), absent DPOAEs in the lower frequency range, and considerably weaker if present at all in the higher-frequency range in $Ca_v\beta_2^{-/-}$ mice (gray; $n = 10$). The markers represent data points of measurements from individual mice. **E, F**, Representative contrast enhanced transmission images of the apical organ of Corti of WT (**E**) and $Ca_v\beta_2^{-/-}$ (**F**) mice. Three rows of intact outer hair cells with V-shaped hair bundles are present in both WT and $Ca_v\beta_2^{-/-}$ mice at 4 weeks of age (arrowheads).

which could not be observed in WT (Fig. 4*F*). In line with this finding, many $Ca_v\beta_2^{-/-}$ IHCs but none of WT IHCs exhibited slowly activating outward currents during long depolarizations (500 ms, Cs^+ -based pipette solution) (Fig. 4*L*), which were

blocked by the specific SK channel blocker apamin (100 nM, added to the extracellular solution and constantly used for quantifying Ca^{2+} currents in $Ca_v\beta_2^{-/-}$ IHCs) (Figs. 1, 2). Together, the data indicate an impaired IHC development in the absence of $Ca_v\beta_2$.

The profound hearing impairment in $Ca_v\beta_2^{-/-}$ mice involves deficits in cochlear amplification and sound encoding

Auditory systems function was first studied at the level of population responses by recordings of ABRs and DPOAE in 3- to 4-week-old mice. ABRs were only observed with strong stimuli (clicks exceeding 90 dB) in $Ca_v\beta_2^{-/-}$ mice, whereas they were readily elicited by weak tone bursts or clicks in WT mice (Fig. 5*A, B*). Thus, the hearing impairment of $Ca_v\beta_2^{-/-}$ mice was profound but not as complete as in $\alpha 1D^{-/-}$ mice in which we did not obtain any ABRs (Fig. 5*A*). Outer hair cells (OHCs) were present at 4 weeks of age, as demonstrated by Figure 5, *E* and *F*, for the apex of the cochlea, in which OHC degeneration is first observed in $\alpha 1D^{-/-}$ mice (Engel et al., 2006). Inspection of phalloidin-stained hair cells in all cochlear turns at 8 weeks of age provided additional evidence for the presence of OHCs throughout the cochlea of $Ca_v\beta_2^{-/-}$ mice (our unpublished data). However, DPOAEs, reporting cochlear amplification by OHCs and readily observed in WT mice, were rarely found in 3- to 4-week-old $Ca_v\beta_2^{-/-}$ mice (Fig. 5*C, D*) (2 of 10 investigated ears, then having reduced amplitudes).

To better understand the consequences of the reduced Ca^{2+} channel number and RRP size at the ribbon synapses of $Ca_v\beta_2^{-/-}$ IHCs, we performed extracellular recordings using microelectrodes that were stereotactically targeted to the cochlear nucleus and auditory nerve (Taberner and Liberman, 2005; Strenzke et al., 2009). Sound-driven single-neuron activity was scarce and found only at high sound intensities (>100 dB SPL). We observed different discharge patterns reflecting firing of the various cell types (supplemental Fig. 4, available at www.jneurosci.org as supplemental material) but focused our analysis on units that most likely represented auditory nerve fibers (and are referred to as auditory nerve fibers in Fig. 6), based on their discharge pattern and the electrode position. Fre-

quency tuning, readily observed in wild-type units, was broad in $Ca_v\beta_2^{-/-}$ mice, which is consistent with the lack of DPOAEs attributable to defective cochlear amplification. Tone bursts were used for stimulation of sound-responsive neurons at maximal

speaker output (on average 10 dB above threshold) at the manually chosen best frequency in $Ca_v\beta_2^{-/-}$ mice and at 30 dB above threshold and characteristic frequency in WT mice. PSTHs (Fig. 6B,C) revealed that peak and adapted spike rates were reduced by ~60 and 70%, respectively, with slightly faster spike rate adaptation in $Ca_v\beta_2^{-/-}$ mice [time constant, 4.6 ± 0.9 ms ($n = 21$ units of $Ca_v\beta_2^{-/-}$ mice) vs 7.8 ± 0.9 ms ($n = 30$ units of WT mice); $p < 0.05$]. Spontaneous spiking activity was less reduced (Fig. 6C) (supplemental Fig. 4, available at www.jneurosci.org as supplemental material). Unequal absolute stimulation levels were chosen because saturation of the spike rate-sound pressure level functions of most wild-type auditory nerve fibers is expected for sound pressure levels of 20 dB greater than threshold (Fig. 6D) (Taberner and Liberman, 2005), and noise damage was feared for the stimuli exceeding 100 dB SPL. When matching the stimulus levels relative to threshold for a subset of $Ca_v\beta_2^{-/-}$ and WT units, the reduction in rates only amounted to ~40% (Fig. 6B, inset). Together, these findings confirmed that pre-synaptic IHC exocytosis of $Ca_v\beta_2^{-/-}$ mice supports residual sound encoding.

Discussion

This study demonstrates an essential role of $Ca_v\beta_2$ for auditory function at the cellular and systems' levels. $Ca_v\beta_2$ is critical for ensuring the large number of Ca^{2+} channels present at normal hair cell synapses, which is required for proper sound encoding. Absence of $Ca_v\beta_2$ reduces the number of synaptic Ca^{2+} channels, which still couple to exocytosis, but cannot support the typically found high rates of hair cell transmitter release and auditory nerve fiber spiking. In addition, $Ca_v\beta_2$ is required for normal postnatal differentiation of IHCs probably by ensuring neonatal, regenerative Ca^{2+} signaling. Finally, we found a defect of OHC-mediated cochlear amplification in $Ca_v\beta_2^{-/-}$ mice, which requires additional investigation.

$Ca_v\beta_2$ is required for normal $Ca_v1.3$ abundance at hair cell synapses and hearing

This study focused on the role of $Ca_v\beta_2$ in sound encoding at the IHC–spiral ganglion afferent synapse. However, the phenotype of $Ca_v\beta_2^{-/-}$ mice also included a deficit of cochlear sound amplification as demonstrated by the lack of otoacoustic emissions in most animals and the deficiency of frequency tuning in single auditory neuron recordings. Because OHCs were present, we propose an OHC dysfunction, whose mechanism remains to be elucidated. The impairment of mechanical amplification cannot fully explain the observed elevation of auditory threshold by 70 dB or greater, because amplification by OHCs accounts for a maximal gain in hearing sensitivity of ~50 dB (Ryan and Dallos, 1975). In conclusion, lack of $Ca_v\beta_2$ causes a profound hearing impairment involving deficits of cochlear amplification and sound encoding at the inner hair cell synapse. This synapse entirely depends on L-type Ca^{2+} channels (Robertson and Paki, 2002; Brandt et al., 2003), which are primarily made of α_1D

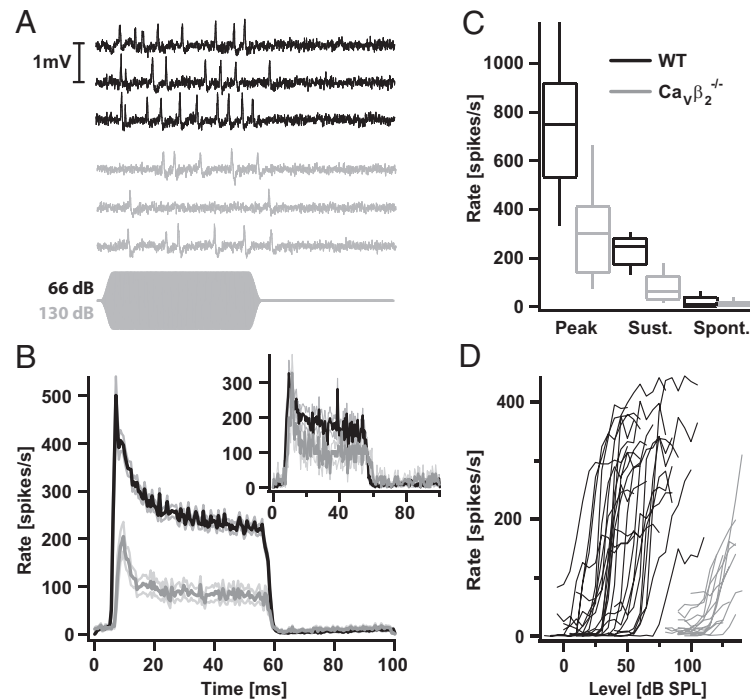


Figure 6. Reduced spike rates in the auditory nerve. **A**, Representative original recording traces of responses of WT (black) and $Ca_v\beta_2^{-/-}$ (gray) mouse auditory nerve fibers to three repetitions of a 50 ms tone burst (depicted below). Mean stimulus intensity for standard PSTHs was 66 dB for WT recordings (30 dB above threshold) and 130 dB for $Ca_v\beta_2^{-/-}$ (maximal speaker output). **B**, Averaged PSTH \pm SEM from WT (black; $n = 55$) and $Ca_v\beta_2^{-/-}$ (gray; $n = 21$) mouse auditory nerve fibers. Inset, Same but applying a stimulus intensity of 10 dB above threshold for all recordings (WT black, $n = 26$; $Ca_v\beta_2^{-/-}$ gray, $n = 10$). **C**, Box-and-whisker plot of peak, sustained (average rate at 40–50 ms after stimulus onset) and spontaneous rates of auditory nerve fibers from WT (black, $n = 55$) and $Ca_v\beta_2^{-/-}$ (gray, $n = 21$) mice. **D**, Spike rates, averaged over the duration of the stimulus, of individual WT (black; $n = 26$) and $Ca_v\beta_2^{-/-}$ (gray; $n = 10$) auditory nerve fibers stimulated at varying sound pressure levels.

subunits (Platzer et al., 2000; Brandt et al., 2003; Dou et al., 2004). Hair cell Ca^{2+} currents and their role in auditory function can be addressed by *in vitro* patch-clamp and *in vivo* recordings. Our study demonstrates that $Ca_v\beta_2$ is expressed and functional in IHCs of the mouse cochlea. This conclusion is based on IHC-specific RT-PCR and functional analysis of $Ca_v\beta_2$ knock-out mice and corrects the previous notion that $Ca_v\beta_2$ is not detectable in the mouse cochlea (Green et al., 1996). Although we also detected mRNAs of $Ca_v\beta_1$ and $Ca_v\beta_3$ in few $Ca_v\beta_2^{-/-}$ and WT IHCs, their role in IHC function is less clear. Our data demonstrate that they do not fully compensate the loss of $Ca_v\beta_2$. The resulting 68% reduction of IHC Ca^{2+} current primarily reflected a reduced number of functional $Ca_v1.3$ channels. We conclude from the presence of Ca^{2+} microdomains that the remaining channels stay clustered. The fact that the average amplitude of the Ca^{2+} microdomains was reduced to a lesser degree (~50%) (Fig. 4C) than the whole-cell Ca^{2+} current (~70%) may be related to the limited sensitivity of our imaging setup, which might be unable to detect the weakest Ca^{2+} microdomains. However, we did not observe a sizable number of synapses lacking a Ca^{2+} microdomain when identifying synapses by labeling ribbons with a fluorescent peptide. Therefore, we argue for a general reduction of the Ca^{2+} channel complement at all IHC synapses and against a selective inactivation of a subset of synapses attributable to the ablation of $Ca_v\beta_2$.

When assuming that the extrasynaptic fraction of Ca^{2+} channels of $Ca_v\beta_2^{-/-}$ and WT IHCs amount to ~30% (see discussion by Brandt et al., 2005), we estimate 30 channels at the average synapse of $Ca_v\beta_2^{-/-}$ IHCs compared with 80 channels at WT synapses [identical to our previous estimate (Brandt et al.,

2005)]. Neither the increase of the Ca^{2+} current by BayK8644 nor the maximal open probability were significantly different in $\text{Ca}_v\beta_2^{-/-}$ IHCs. Therefore, we conclude that the remaining Ca^{2+} current is mostly mediated by $\text{Ca}_v1.3$ channels. Based on the maximal open probability in the presence of BayK8644 and the BayK8644-induced current augmentation, we predict that, in the absence of BayK8644, maximally ~ 10 channels in $\text{Ca}_v\beta_2^{-/-}$ and ~ 40 channels in WT IHCs open simultaneously per active zone during saturating depolarization. Although this represents a substantial reduction, the Ca^{2+} channel complement of $\text{Ca}_v\beta_2^{-/-}$ IHCs still seems sizable. Indeed, the *in vivo* recordings from single auditory neurons—most likely from auditory nerve fibers—indicate that, although auditory sensitivity was very low, a residual sound encoding was maintained in $\text{Ca}_v\beta_2^{-/-}$ mice.

These observations are in line with the hypothesis of a critical role of $\text{Ca}_v\beta$ s in $\text{Ca}_v\alpha_1$ membrane trafficking (Bichet et al., 2000). Although we cannot exclude a $\text{Ca}_v\beta$ -independent membrane expression (Ravindran et al., 2008), we favor the interpretation that the trafficking of the remaining $\text{Ca}_v1.3$ channels was facilitated by other $\text{Ca}_v\beta$ subunits. Consistent with the assumption of functional $\text{Ca}_v1.3$ – $\text{Ca}_v\beta$ complexes in $\text{Ca}_v\beta_2^{-/-}$ IHCs, we did not observe major alterations of Ca^{2+} channel gating. The lack of fast CDI may reflect the lower amplitude of the presynaptic Ca^{2+} domain attributable to the reduced Ca^{2+} influx. Indeed, reducing the WT Ca^{2+} current by decreasing extracellular [Ca^{2+}] led to a reduced fast component of CDI (our unpublished data). The increased rate of slow CDI in $\text{Ca}_v\beta_2^{-/-}$ IHCs seems consistent with the unique ability of $\text{Ca}_v\beta_{2a}$ or $\text{Ca}_v\beta_{2e}$ to inhibit CDI (Takahashi et al., 2003; Cui et al., 2007). The lack of full compensation of $\text{Ca}_v\beta_2$ function by the remaining $\text{Ca}_v\beta$ s may be related to lower expression levels of the other remaining $\text{Ca}_v\beta$ s, as indicated by the low percentage of positive samples in single-cell RT-PCR and/or to the high efficacy in $\text{Ca}_v1.3$ membrane trafficking of the palmitoylated $\text{Ca}_v\beta_2$ subunit (Chien et al., 1998). Obviously, the straight knock-out of $\text{Ca}_v\beta_2$ is effective already during differentiation of the hair cell, leaving room for compensation or confounding developmental effects. Therefore, it remains possible that acute interference with $\text{Ca}_v\beta_2$ function may result in less or more drastic effects.

Our study further highlights the requirement of intact Ca^{2+} signaling for sensory cell development and maintenance (Ball et al., 2002; Brandt et al., 2003; Jalkanen et al., 2006; Nemzou et al., 2006; Wycisk et al., 2006). The altered localization and function of BK channels may represent a phenotype intermediate between normal and $\alpha 1D^{-/-}$ IHCs. BK channels of normal IHCs show a peculiarly negative voltage range of activation and do not, or very little, depend on voltage-gated Ca^{2+} influx (Marcotti et al., 2004; Thurm et al., 2005). Our as yet unexplained finding of a substantial depolarized shift in BK activation makes $\text{Ca}_v\beta_2^{-/-}$ IHCs an interesting object to further study the regulation of these unique channel properties. It is not trivial to estimate the impact of BK current alteration in $\text{Ca}_v\beta_2^{-/-}$ IHCs on hearing. Genetic deletion of BK channels does not cause an increase in auditory thresholds at least before 8 weeks of age (Ruttiger et al., 2004; Oliver et al., 2006). However, a reduction in single auditory nerve fiber spike rates and deteriorated temporal precision of sound encoding were found in these mice (Oliver et al., 2006). Although impaired temporal precision was attributed to the disturbed timing of the receptor potential of the BK deficient IHCs, a potential postsynaptic contribution to the decreased spike rate could not be excluded (Oliver et al., 2006).

Functional coupling $\text{Ca}_v1.3$ channels to synaptic vesicle release in IHCs

$\text{Ca}_v\beta$ linking the Ca^{2+} channel to the docked vesicle via interaction with RIM (Kiyonaka et al., 2007) represented an attractive hypothesis for enabling a “ Ca^{2+} nanodomain control” of vesicle release at the IHC synapse (Brandt et al., 2005; Moser et al., 2006; Goutman and Glowatzki, 2007). Does the nanoscale topography of Ca^{2+} channels and docked vesicles require $\text{Ca}_v\beta_2$? Unfortunately, addressing this question is complicated by the strong reduction of functional Ca^{2+} channels in the absence of $\text{Ca}_v\beta_2$. However, although reduced, exocytosis appeared still coupled to Ca^{2+} influx in a manner that argued against Ca^{2+} microdomain control. In this scenario, the supralinear nature of the intrinsic Ca^{2+} dependence of exocytosis (Beutner et al., 2001) would be revealed as a relatively stronger reduction of exocytosis when compared with the decrease in Ca^{2+} current (Augustine et al., 1991). However, we observed a comparable change of both quantities, which rather argues for a Ca^{2+} nanodomain control to be at work also in $\text{Ca}_v\beta_2^{-/-}$ IHCs. This notion is further supported by the unaltered low sensitivity to the slow Ca^{2+} chelator EGTA and seems compatible with a scenario in which fewer Ca^{2+} channels still closely colocalize with release ready vesicles. Relating the observed changes of *in vivo* spike rates to the reduced Ca^{2+} channel numbers and rates of exocytosis found *in vitro* is difficult, not only because of the different sound sensitivities of $\text{Ca}_v\beta_2^{-/-}$ and wild-type neurons that forced us use different sound intensities for suprathreshold stimulation. Nevertheless, we argue that sound encoding does occur with one-third of the normal Ca^{2+} channel complement and RRP size. Moreover, comparison of the kinetics of RRP exocytosis and postsynaptic spike rate adaptation suggest that RRP consumption causing rapid peripheral auditory adaptation (Furukawa and Matsuura, 1978; Moser and Beutner, 2000; Spassova et al., 2004; Goutman and Glowatzki, 2007) proceeds at normal or even faster pace. This supports the notion that Ca^{2+} influx–exocytosis coupling was not disturbed for the remaining RRP.

References

- Augustine GJ, Adler EM, Charlton MP (1991) The calcium signal for transmitter secretion from presynaptic nerve terminals. *Ann N Y Acad Sci* 635:365–381.
- Ball SL, Powers PA, Shin HS, Morgans CW, Peachey NS, Gregg RG (2002) Role of the beta(2) subunit of voltage-dependent calcium channels in the retinal outer plexiform layer. *Invest Ophthalmol Vis Sci* 43:1595–1603.
- Beutner D, Moser T (2001) The presynaptic function of mouse cochlear inner hair cells during development of hearing. *J Neurosci* 21:4593–4599.
- Beutner D, Voets T, Neher E, Moser T (2001) Calcium dependence of exocytosis and endocytosis at the cochlear inner hair cell afferent synapse. *Neuron* 29:681–690.
- Bichet D, Cornet V, Geib S, Carlier E, Volsen S, Hoshi T, Mori Y, De Waard M (2000) The I–II loop of the Ca^{2+} channel $\alpha 1$ subunit contains an endoplasmic reticulum retention signal antagonized by the beta subunit. *Neuron* 25:177–190.
- Brandt A, Striessnig J, Moser T (2003) $\text{Ca}_v1.3$ channels are essential for development and presynaptic activity of cochlear inner hair cells. *J Neurosci* 23:10832–10840.
- Brandt A, Khimich D, Moser T (2005) Few $\text{Ca}_v1.3$ channels regulate the exocytosis of a synaptic vesicle at the hair cell ribbon synapse. *J Neurosci* 25:11577–11585.
- Brandt N, Kuhn S, Münkner S, Braig C, Winter H, Blin N, Vonthein R, Knipper M, Engel J (2007) Thyroid hormone deficiency affects postnatal spiking activity and expression of Ca^{2+} and K^{+} channels in rodent inner hair cells. *J Neurosci* 27:3174–3186.
- Catterall WA, Perez-Reyes E, Snutch TP, Striessnig J (2005) International Union of Pharmacology. XLVIII. Nomenclature and structure-function relationships of voltage-gated calcium channels. *Pharmacol Rev* 57:411–425.

- Chien AJ, Gao T, Perez-Reyes E, Hosey MM (1998) Membrane targeting of L-type calcium channels. Role of palmitoylation in the subcellular localization of the beta2a subunit. *J Biol Chem* 273:23590–23597.
- Cui G, Meyer AC, Calin-Jageman I, Neef J, Haeseleer F, Moser T, Lee A (2007) Ca^{2+} -binding proteins tune Ca^{2+} -feedback to Cav1.3 channels in mouse auditory hair cells. *J Physiol* 585:791–803.
- Dolphin AC (2003) Beta subunits of voltage-gated calcium channels. *J Bioenerg Biomembr* 35:599–620.
- Dou H, Vazquez AE, Namkung Y, Chu H, Cardell EL, Nie L, Parson S, Shin HS, Yamoah EN (2004) Null mutation of alpha1D Ca^{2+} channel gene results in deafness but no vestibular defect in mice. *J Assoc Res Otolaryngol* 5:215–226.
- Engel J, Braig C, Rüttiger L, Kuhn S, Zimmermann U, Blin N, Sausbier M, Kalbacher H, Münkner S, Rohbock K, Ruth P, Winter H, Knipper M (2006) Two classes of outer hair cells along the tonotopic axis of the cochlea. *Neuroscience* 143:837–849.
- Frank T, Khimich D, Neef A, Moser T (2009) Mechanisms contributing to synaptic Ca^{2+} signals and their heterogeneity in hair cells. *Proc Natl Acad Sci U S A* 106:4483–4488.
- Fuchs PA (2005) Time and intensity coding at the hair cell's ribbon synapse. *J Physiol* 566:7–12.
- Furukawa T, Matsuura S (1978) Adaptive rundown of excitatory postsynaptic potentials at synapses between hair cells and eight nerve fibres in the goldfish. *J Physiol* 276:193–209.
- Goutman JD, Glowatzki E (2007) Time course and calcium dependence of transmitter release at a single ribbon synapse. *Proc Natl Acad Sci U S A* 104:16341–16346.
- Green GE, Khan KM, Beisel DW, Drescher MJ, Hatfield JS, Drescher DG (1996) Calcium channel subunits in the mouse cochlea. *J Neurochem* 67:37–45.
- Hafidi A, Beurq M, Dulon D (2005) Localization and developmental expression of BK channels in mammalian cochlear hair cells. *Neuroscience* 130:475–484.
- Hidalgo P, Neely A (2007) Multiplicity of protein interactions and functions of the voltage-gated calcium channel beta-subunit. *Cell Calcium* 42:389–396.
- Jalkanen R, Mäntyjärvi M, Tobias R, Isosomppi J, Sankila EM, Alitalo T, Bech-Hansen NT (2006) X linked cone-rod dystrophy, *CORDX3*, is caused by a mutation in the *CACNA1F* gene. *J Med Genet* 43:699–704.
- Katz E, Elgoyhen AB, Gómez-Casati ME, Knipper M, Vetter DE, Fuchs PA, Glowatzki E (2004) Developmental regulation of nicotinic synapses on cochlear inner hair cells. *J Neurosci* 24:7814–7820.
- Khimich D, Nouvian R, Pujol R, Tom Dieck S, Egner A, Gundelfinger ED, Moser T (2005) Hair cell synaptic ribbons are essential for synchronous auditory signalling. *Nature* 434:889–894.
- Kiyonaka S, Wakamori M, Miki T, Uriu Y, Nonaka M, Bito H, Beedle AM, Mori E, Hara Y, De Waard M, Kanagawa M, Itakura M, Takahashi M, Campbell KP, Mori Y (2007) RIM1 confers sustained activity and neurotransmitter vesicle anchoring to presynaptic Ca^{2+} channels. *Nat Neurosci* 10:691–701.
- Kros CJ, Crawford AC (1990) Potassium currents in inner hair cells isolated from the guinea-pig cochlea. *J Physiol* 421:263–291.
- Kros CJ, Ruppersberg JP, Rüsch A (1998) Expression of a potassium current in inner hair cells during development of hearing in mice. *Nature* 394:281–284.
- Marcotti W, Johnson SL, Holley MC, Kros CJ (2003) Developmental changes in the expression of potassium currents of embryonic, neonatal and mature mouse inner hair cells. *J Physiol* 548:383–400.
- Marcotti W, Johnson SL, Kros CJ (2004) Effects of intracellular stores and extracellular Ca^{2+} on Ca^{2+} -activated K^{+} currents in mature mouse inner hair cells. *J Physiol* 557:613–633.
- Michna M, Knirsch M, Hoda JC, Muenkner S, Langer P, Platzer J, Striessnig J, Engel J (2003) Cav1.3 (alpha1D) Ca^{2+} currents in neonatal outer hair cells of mice. *J Physiol* 553:747–758.
- Moser T, Beutner D (2000) Kinetics of exocytosis and endocytosis at the cochlear inner hair cell afferent synapse of the mouse. *Proc Natl Acad Sci U S A* 97:883–888.
- Moser T, Neef A, Khimich D (2006) Mechanisms underlying the temporal precision of sound coding at the inner hair cell ribbon synapse. *J Physiol* 576:55–62.
- Nemzou RM, Bulankina AV, Khimich D, Giese A, Moser T (2006) Synaptic organization in Cav1.3 Ca^{2+} channel deficient cochlear hair cells. *Neuroscience* 141:1849–1860.
- Oliver D, Taberner AM, Thurm H, Sausbier M, Arntz C, Ruth P, Fakler B, Liberman MC (2006) The role of BKCa channels in electrical signal encoding in the mammalian auditory periphery. *J Neurosci* 26:6181–6189.
- Platzer J, Engel J, Schrott-Fischer A, Stephan K, Bova S, Chen H, Zheng H, Striessnig J (2000) Congenital deafness and sinoatrial node dysfunction in mice lacking class D L-type Ca^{2+} channels. *Cell* 102:89–97.
- Pyott SJ, Glowatzki E, Trimmer JS, Aldrich RW (2004) Extrasynaptic localization of inactivating calcium-activated potassium channels in mouse inner hair cells. *J Neurosci* 24:9469–9474.
- Ravindran A, Lao QZ, Harry JB, Abrahami P, Kobrinisky E, Soldatov NM (2008) Calmodulin-dependent gating of $\text{Ca}_v1.2$ calcium channels in the absence of $\text{Ca}_v\beta$ subunits. *Proc Natl Acad Sci U S A* 105:8154–8159.
- Roberts WM, Jacobs RA, Hudspeth AJ (1990) Colocalization of ion channels involved in frequency selectivity and synaptic transmission at presynaptic active zones of hair cells. *J Neurosci* 10:3664–3684.
- Robertson D, Paki B (2002) Role of L-type Ca^{2+} channels in transmitter release from mammalian inner hair cells. II. Single-neuron activity. *J Neurophysiol* 87:2734–2740.
- Roux I, Safieddine S, Nouvian R, Grati M, Simmler MC, Bahloul A, Perfettini I, Le Gall M, Rostaing P, Hamard G, Triller A, Avan P, Moser T, Petit C (2006) Otoferlin, defective in a human deafness form, is essential for exocytosis at the auditory ribbon synapse. *Cell* 127:277–289.
- Rüttiger L, Sausbier M, Zimmermann U, Winter H, Braig C, Engel J, Knirsch M, Arntz C, Langer P, Hirt B, Müller M, Köpsschall I, Pfister M, Münkner S, Rohbock K, Pfaff I, Rüsch A, Ruth P, Knipper M (2004) Deletion of the Ca^{2+} -activated potassium (BK) alpha-subunit but not the BKbeta1-subunit leads to progressive hearing loss. *Proc Natl Acad Sci U S A* 101:12922–12927.
- Ryan A, Dallos P (1975) Effect of absence of cochlear outer hair cells on behavioural auditory threshold. *Nature* 253:44–46.
- Sendin G, Bulankina AV, Riedel D, Moser T (2007) Maturation of ribbon synapses in hair cells is driven by thyroid hormone. *J Neurosci* 27:3163–3173.
- Spassova MA, Avissar M, Furman AC, Crumling MA, Saunders JC, Parsons TD (2004) Evidence that rapid vesicle replenishment of the synaptic ribbon mediates recovery from short-term adaptation at the hair cell afferent synapse. *J Assoc Res Otolaryngol* 5:376–390.
- Strenzke N, Chanda S, Kopp-Scheinpflug C, Khimich D, Reim K, Bulankina AV, Neef A, Wolf F, Brose N, Xu-Friedman MA, Moser T (2009) Complexin-I is required for high-fidelity transmission at the endbulb of held auditory synapse. *J Neurosci* 29:7991–8004.
- Taberner AM, Liberman MC (2005) Response properties of single auditory nerve fibers in the mouse. *J Neurophysiol* 93:557–569.
- Takahashi SX, Mittman S, Colecraft HM (2003) Distinctive modulatory effects of five human auxiliary beta2 subunit splice variants on L-type calcium channel gating. *Biophys J* 84:3007–3021.
- Thurm H, Fakler B, Oliver D (2005) Ca^{2+} -independent activation of BKCa channels at negative potentials in mammalian inner hair cells. *J Physiol* 569:137–151.
- Van Petegem F, Clark KA, Chatelain FC, Minor DL Jr (2004) Structure of a complex between a voltage-gated calcium channel beta-subunit and an alpha-subunit domain. *Nature* 429:671–675.
- Van Petegem F, Duderstadt KE, Clark KA, Wang M, Minor DL Jr (2008) Alanine-scanning mutagenesis defines a conserved energetic hotspot in the CaValpha1 AID-CaVbeta interaction site that is critical for channel modulation. *Structure* 16:280–294.
- Wycisk KA, Zeitz C, Feil S, Wittmer M, Forster U, Neidhardt J, Wissinger B, Zrenner E, Wilke R, Kohl S, Berger W (2006) Mutation in the auxiliary calcium-channel subunit *CACNA2D4* causes autosomal recessive cone dystrophy. *Am J Hum Genet* 79:973–977.
- Yang PS, Alseikhan BA, Hiel H, Grant L, Mori MX, Yang W, Fuchs PA, Yue DT (2006) Switching of Ca^{2+} -dependent inactivation of $\text{Ca}_v1.3$ channels by calcium binding proteins of auditory hair cells. *J Neurosci* 26:10677–10689.
- Zenisek D, Horst NK, Merrifield C, Sterling P, Matthews G (2004) Visualizing synaptic ribbons in the living cell. *J Neurosci* 24:9752–9759.